

3D Simulations of M 7 Earthquakes on the Wasatch Fault, Utah, Part I: Long-Period (0–1 Hz) Ground Motion

by D. Roten,* K. B. Olsen, J. C. Pechmann, V. M. Cruz-Atienza, and H. Magistrale

Abstract We predict ground motions in the Salt Lake basin (SLB) during M 7 earthquakes on the Salt Lake City segment of the Wasatch fault (WFSLC). First we generate a suite of realistic source representations by simulating the spontaneous rupture process on a planar, vertical fault with the staggered-grid split-node finite-difference (FD) method. The initial distribution of shear stress is the sum of both a regional depth-dependent shear stress appropriate for a dipping, normal fault and a stochastically generated residual shear stress field associated with previous ruptures. The slip-rate histories from the spontaneous rupture scenarios are projected onto a detailed 3D model geometry of the WFSLC that we developed based on geological observations. Next, we simulate 0- to 1-Hz wave propagation from six source models with a 3D FD code, using the most recent version of the Wasatch Front Community Velocity model. Horizontal spectral accelerations at two seconds (2-s SAs) reveal strong along-strike rupture direction effects for unilateral ruptures, as well as significant amplifications by the low-velocity sediments on the hanging-wall side of the fault. For ruptures nucleating near the southern end of the segment, we obtain 2-s SAs of up to $1.4g$ near downtown SLC, caused by a combination of rupture-direction and basin-edge effects. Average 3-s SAs and 2-s SAs from the six scenarios are generally consistent with values predicted by four next-generation attenuation models.

Online Material: Supplementary figures of spectral acceleration and animation of wave propagation.

Introduction

The Wasatch fault in northern and central Utah is a major normal fault that separates the Salt Lake basin (SLB) to the west from the Wasatch Range to the east. The Salt Lake City segment of the Wasatch fault (WFSLC) represents the most obvious source of seismic hazard to the SLB, a major metropolitan area inhabited by more than a million people. Paleoseismological studies (Black *et al.*, 1995; McCalpin and Nishenko, 1996; McCalpin and Nelson, 2000) have shown that the WFSLC ruptures during large $M \sim 7$ surface-faulting earthquakes with an average return interval of 1350 ± 200 yr and that the last such event occurred approximately 1230 ± 60 yr B.P. Based on these findings, McCalpin and Nelson (2000) have estimated the probability of an $M \sim 7$ earthquake occurring during the next 100 yr to be 16%; Wong, Silva, Olig, *et al.* (2002) have estimated that the probability for the next 50 yr is 6%–9%.

Worldwide, there are few near-fault strong ground-motion records from $M \geq 6$ normal-faulting earthquakes,

and no records for $M \geq 7$ normal-faulting earthquakes (Chiou *et al.*, 2008; Campbell and Bozorgnia, 2008). As a result, there is a large uncertainty associated with the ground motions expected from future M 7 earthquakes on the WFSLC.

Adding to this uncertainty are the soft sediments of the SLB, which are more than 1-km deep in some places. Such unconsolidated deposits may significantly amplify the seismic ground motion during large earthquakes and contribute drastically to the loss of life and property, as has been demonstrated repeatedly during earthquakes elsewhere. Nonlinear soil behavior, on the other hand, may lead to a deamplification of strong ground motion, especially at higher frequencies (> 1 Hz).

It is vital to gain a quantitative understanding of the ground motion expected from future large earthquakes on the WFSLC. In this study, we address this issue by performing 0- to 1-Hz 3D finite-difference (FD) simulations of wave propagation in the SLB based on a detailed velocity model, a realistic fault geometry, and rupture models derived from spontaneous rupture simulations.

*Now at Swiss Seismological Service, ETH Zürich, Switzerland.

The FD simulations presented in this paper are limited to frequencies of 1.0 Hz and lower. However, the long-period ground motions derived from these FD simulations provide the basis for deriving 0- to 10-Hz synthetic ground motions for the SLB using scattering operators and fully nonlinear 1D simulations. The 0- to 10-Hz ground-motion predictions will be presented in a separate publication (Part II).

Background

The most recent studies of strong ground motion in the SLB were performed by Wong, Silva, Olig, *et al.* (2002), Wong, Silva, Gregor, *et al.* (2002), and Solomon *et al.* (2004). They used a methodology that combines aspects of finite earthquake-source modeling with the bandlimited white-noise ground-motion model, random vibration theory, and an equivalent-linear soil response calculation. Their results were consistent with previous studies by Adan and Rollins (1993) and Wong and Silva (1993), which accounted for near-surface site-effects in a similar manner. Wong, Silva, Olig, *et al.* (2002), Wong, Silva, Gregor, *et al.* (2002), and Solomon *et al.* (2004) predicted 1.0-s spectral accelerations (1-s SAs) exceeding $1.3g$ on the hanging-wall side of the southern WFSLC, which they attributed to amplification by the relatively deep basin sediments there. Because all of these studies treated the site amplification in 1D, they could not account for effects caused by the 3D structure of the basin. However, numerous theoretical studies of seismic-wave propagation in 2D and 3D structures have shown that basin walls play a major role in amplifying seismic waves (e.g., Bard and Bouchon, 1980a, 1980b; Kawase, 1996; Olsen and Archuleta, 1996; Olsen *et al.*, 2009). Evidence for basin-edge-generated waves has also been found in many weak ground motion records (e.g., Field, 1996; Frankel *et al.*, 2001; Cornou *et al.*, 2003; Roten *et al.*, 2008).

The important influence of the SLB walls on seismic response was first reported by Benz and Smith (1988), Murphy *et al.* (1988), and Hill *et al.* (1990) based on 2D numerical simulations. Increases in computational power allowed Olsen *et al.* (1995), Olsen and Schuster (1995), and Olsen *et al.* (1996) to extend the numerical simulations to 3D. All of these 2D and 3D studies revealed large spectral amplifications in the modeled frequency range (< 1.2 – 2.7 Hz), but they used rather simple models of the SLB and constrained the minimum shear-wave velocity to 410 – 2020 $\text{m}\cdot\text{s}^{-1}$ due to limitations in computational resources. A further limitation of these early numerical simulations was the representation of the seismic sources, which were modeled as horizontally or vertically incident plane waves, line or point sources, or 2D normal-faulting earthquakes with uniform displacement.

More recently, O'Connell *et al.* (2007) used a 3D finite-element method to simulate spontaneous rupture on dipping faults. They also studied the effect of a bimaterial contrast across the fault by modeling the Teton normal fault in Wyoming, which, like the Wasatch fault, forms a boundary between bedrock on the footwall side and sediments on the

hanging-wall side. The simulations of O'Connell *et al.* (2007), which were performed in the frequency band 0–1 Hz, produced the highest peak-ground velocities on the lower-velocity sediments on the hanging-wall side of the fault. This result is qualitatively in agreement with the findings of Wong, Silva, Olig, *et al.* (2002), Wong, Silva, Gregor, *et al.* (2002), and Solomon *et al.* (2004) for the southern WFSLC, where they predicted the highest 1-s SAs on the hanging-wall side. But farther north along the central WFSLC, where there are sediments on both sides of the fault, Wong, Silva, Olig, *et al.* (2002) and Wong, Silva, Gregor, *et al.* (2002) predicted the largest 1-s SAs (1.1 to $> 1.3g$) to be on the footwall side of the fault. The simulations of O'Connell *et al.* (2007) did not predict such amplifications on the footwall side, because sediments were only present on the hanging-wall side in their velocity model. These results demonstrate the need to perform realistic 3D numerical simulations using an accurate velocity model of the SLB and a detailed source representation in order to predict ground motions during future $M \sim 7$ earthquakes on the WFSLC.

Geophysical Model and Fault Geometry

We use the Wasatch fault community velocity model (WFCVM, Version 3c; Magistrale *et al.*, 2009) for our simulations. The model includes detailed site-response units based on surficial geology and shallow shear-wave data (McDonald and Ashland, 2008) atop rule-based representations of basins along the Wasatch front, all embedded in a 3D crust derived from sonic logs and seismic tomography. It is conceptually similar to the SCEC velocity model created for southern California (Magistrale *et al.*, 2000).

Because the Wasatch fault forms the boundary between the SLB deposits on the hanging-wall side to the west and the bedrock on the footwall side to the east, the shallow geometry of the WFSLC is already partly defined in the WFCVM. The fault structure in the WFCVM is mostly based on the work of Bruhn *et al.* (1992), who modeled the near-surface dips of different fault sections of the WFSLC based on field measurements and on the assumption that most fault sections intersect along lines that have the same azimuth as the slip vector, which is 240° . We used this fault model as a basis to generate a realistic 3D model of the WFSLC to ensure that the fault model is consistent with the geometry of the basins.

The surface trace of our WFSLC model (thick line in Fig. 1) follows the general trends of the mapped Holocene surface faulting on this segment, which consists of three enechelon sections separated by left steps: the Warm Springs fault (WSF), the East Bench fault (EBF) and the Cottonwood section (CS; Fig. 1). North of downtown Salt Lake City (SLC), our fault model follows the easternmost of the two branches of the Warm Springs section of the fault, as this branch appears to be the primary branch. We connected the southern end of the WSF to the northern end of the EBF by a straight tear fault in order to keep the fault model contiguous. The dip of the tear fault (65°) was modeled using the same

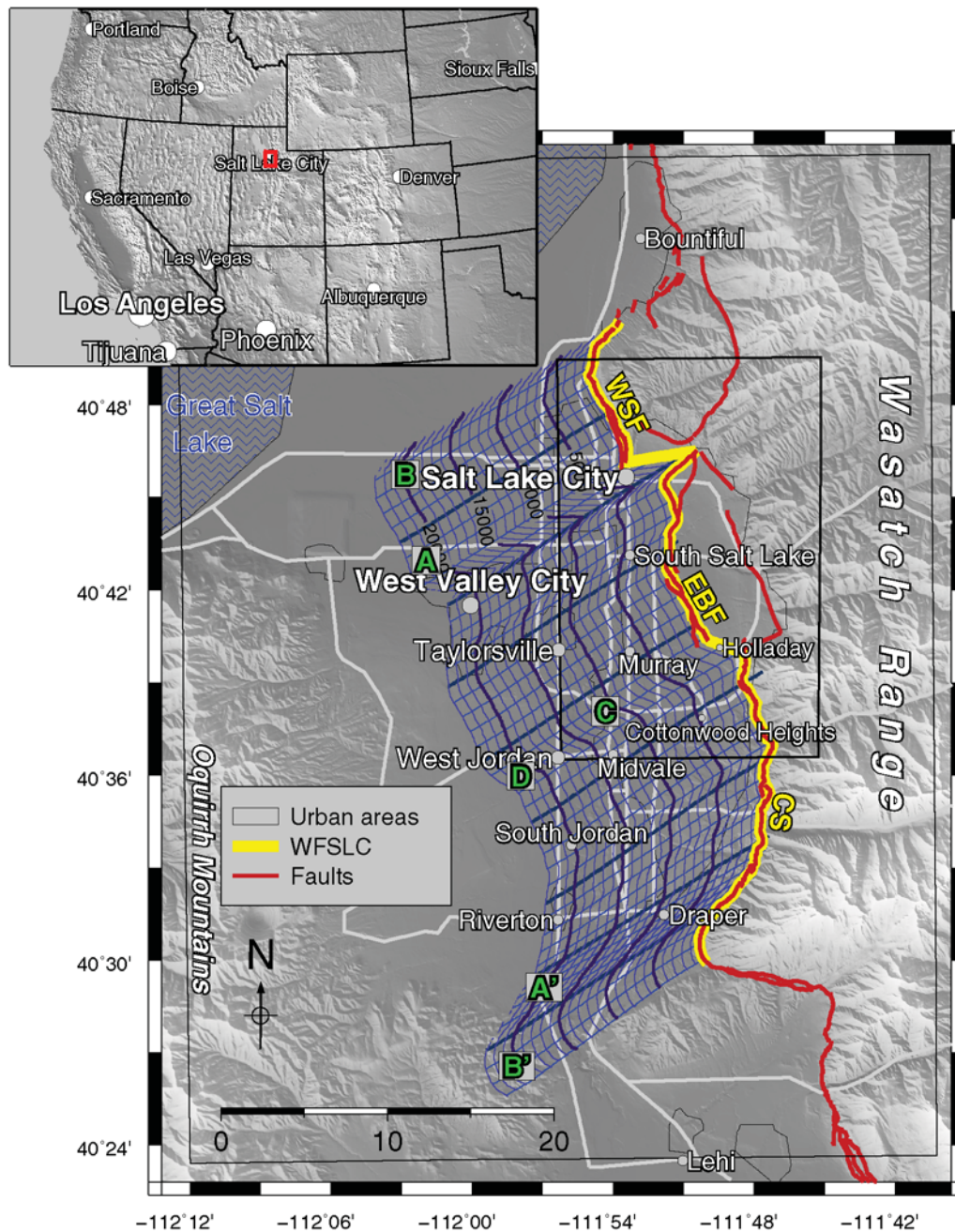


Figure 1. Map of the Salt Lake basin showing known Quaternary surface faulting on the Wasatch fault zone and the surface trace of the WFSLC model. The mesh shows the 3D structure of the WFSLC with along-strike and along-dip distances in 1000-m contours. Letters represent the epicenter locations in the six rupture models. The outer rectangle shows the extent of the computational model used for FD simulations; the inner rectangle indicates the region shown in Figure 2. WSF, Warm Springs fault; EBF, East Bench fault; CS, Cottonwood section.

assumptions made by Bruhn *et al.* (1992). Further south near Holladay, the WFSLC model bridges another gap in the known Holocene fault trace, using a connecting fault that dips 30° to the south-southwest as in the Bruhn *et al.* (1992) model. South of this connecting fault, our fault model follows the narrow zone of surface scarps along the Wasatch Range front until the WFSLC ends at the Traverse Mountains barrier (Machette *et al.*, 1991).

We extrapolated the shallow fault geometry to greater depth using a dip of 50° and a slip azimuth of 240° , consistent

with the average values in the Bruhn *et al.* (1992) WFSLC model. As a result, the geometry of the surface trace of the fault is generally preserved with increasing depth. The grid lines in Figure 1 show the surface projection of the fault mesh with along-strike and along-dip distances in 1000-m contours. Down-dip distances were measured along the surface of the fault in the slip direction. Along-strike distances were defined on the surface trace of the fault and projected to greater depth in the slip direction. We consider our 3D WFSLC model to be plausible based on the available geological information.

However, the details of this model are uncertain due to the lack of data on the fault geometry at depth and the connections, if any, across the two left steps in the surface trace. We chose to connect both stepovers with faults because published dynamic rupture models do not support rupture jumps across 2- to 4-km fault discontinuities, at least on dip-slip faults (Magistrale and Day, 1999). The simulated ground motions would likely be different if the ruptures did, in fact, jump across these stepovers.

Figure 2 (left) is a fence diagram showing the shear-wave velocity in the central SLB and the fault geometry of this region. The unconsolidated and semiconsolidated deposits reach a combined thickness of more than 1000 m on the hanging-wall side of the fault to the north, while the footwall side consists mostly of bedrock. In the central part of the area shown in Figure 2, the fault runs west of the mountain front, cutting through the low-velocity sediments. Consequently, we also find unconsolidated sediments on the footwall side in this area, although the sediment thickness is much greater on the hanging-wall side. Figure 2 (right) is a map showing the average shear-wave velocity in the top 30 m, V_{S30} . In the northwestern part of the SLB on the hanging-wall side of the WSF and EBF, V_{S30} is mostly between 200 and 300 $\text{m}\cdot\text{s}^{-1}$. The V_{S30} is generally higher on the hanging-wall side of the CS in the southern part of the SLB, where it ranges between 300 and 600 $\text{m}\cdot\text{s}^{-1}$. In the sediments on the footwall side of the EBF in the central SLB, the V_{S30} is between 400 and 700 $\text{m}\cdot\text{s}^{-1}$. We find larger V_{S30} of more than 600 $\text{m}\cdot\text{s}^{-1}$ adjacent to the fault on the footwall side of the WSF and CS. The color map in Figure 2 (right) saturates at 1000 $\text{m}\cdot\text{s}^{-1}$,

but we note that the V_{S30} in the bedrock is typically $\sim 1450 \text{ m}\cdot\text{s}^{-1}$ everywhere.

Figure 2 (right) also shows the depth to the R_1 interface, which marks the transition from unconsolidated to semiconsolidated sediments (Magistrale *et al.*, 2008). In the northern part of the SLB, the unconsolidated sediments are typically more than 200-m deep, with a maximum depth of 710 m west of the WSF. The R_1 interface is shallower in the southern part of the SLB, where it is typically less than 200 m below the surface except in the Cottonwood Heights area.

Dynamic Rupture Modeling

In order to obtain a suite of realistic rupture models of $M 7$ earthquakes on the Wasatch fault, we perform simulations of spontaneous rupture on a 43 km (along-strike) \times 21 km (downdip) fault with the staggered-grid split-node FD method (Dalguer and Day, 2007). Because the code is limited to rupture simulation on a planar, vertical fault, we adopt a two-step process. In a first step, we simulate the dynamic rupture process on a planar, vertical fault embedded in a 1D model representative of the structure on the hanging-wall side of the fault. Then the moment-rate time histories obtained from the spontaneous rupture simulation on the fault are projected onto the irregular 3D fault model represented by the mesh in Figure 1. In the second step, we simulate the wave propagation resulting from this kinematic rupture model embedded in the heterogeneous 3D structure of the SLB.

We follow a method proposed by Dalguer and Mai (2008) to define depth-dependent initial shear and normal

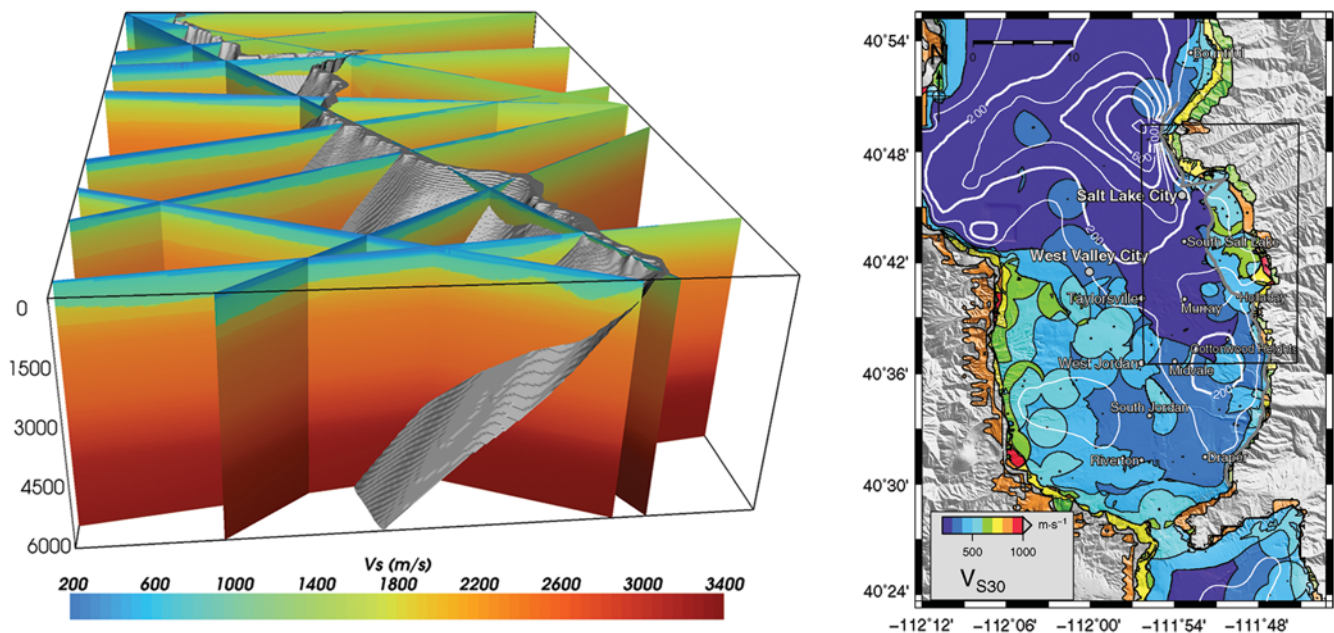


Figure 2. Left: Cross-sections through the WFCVM in the central Salt Lake basin (inner rectangle in Fig. 1) showing the shear-wave velocity ($\text{m}\cdot\text{s}^{-1}$). The gray surface shows the WFSLC model. The depth scale is in meters. Right: V_{S30} for sediments (color coded) and depth to the base of the unconsolidated sediments R_1 (100-m contours).

stress on the fault. In an extensional tectonic regime, the major principal stress σ_1 coincides with the vertical stress and is equivalent to the gravitational load σ_v (Sibson, 1991):

$$\sigma_1(h) = \sigma_v(h) = \int_0^h \rho(z)gz, \quad (1)$$

where ρ is the rock density, h is the depth, and g is Earth's gravitational acceleration. The minor principal stress σ_3 is being lowered due to tectonic extension:

$$\sigma_3 = \sigma_1 - \Delta\sigma, \quad (2)$$

with $\Delta\sigma$ increasing linearly with depth, such that $\Delta\sigma = 0$ at the free surface and $\Delta\sigma = 50$ MPa at 15-km depth. The shear (τ_t) and normal (σ_n) tectonic stresses on a fault of dip θ are thus given by

$$\tau_t = \frac{\sigma_1 - \sigma_3}{2} \sin(2\theta), \quad (3)$$

and

$$\sigma_n = \frac{\sigma_1 + \sigma_3}{2} + \frac{\sigma_1 - \sigma_3}{2} \cos(2\theta). \quad (4)$$

The frictional strength on the fault obeys Coulomb friction and is defined as

$$\tau_c = C + \mu\sigma'_n = C + \mu(\sigma_n + p), \quad (5)$$

where C is the cohesive strength of the fault, and p is the hydrostatic pressure, which increases linearly with depth. The friction coefficient μ is described by a slip-weakening model:

$$\mu(l) = \begin{cases} \mu_s - (\mu_s - \mu_d)l/d_0 & \text{if } l < d_0 \\ \mu_d & \text{if } l \geq d_0, \end{cases} \quad (6)$$

where l is slip. We used a cohesion C of 1 MPa, a static friction coefficient μ_s of 0.67, and a critical slip displacement d_0 of 0.20 m. The dynamic friction coefficient μ_d was set to 0.57 for rupture models A and C and to 0.54 for rupture models B and D. This selection of parameters was found to generate generally subshear rupture propagation and a slip distribution reasonable for an M 7 normal-faulting earthquake in terms of the average and maximum slip (Wells and Coppersmith, 1994).

We generated a heterogeneous stress field τ_r (Ripperger *et al.*, 2007), with a spectral decay that is compatible with seismological observations, using a fractal model with a dimension D of 2.5 and a corner wavenumber k_c of 0.125 km⁻¹ (Mai and Beroza, 2002). Because the initial shear stress on the fault τ_0 is the combination of both the tectonic and residual stress components, we generated τ_0 by simply adding τ_t and τ_r so that its values are bounded by the static and dynamic fault strengths for all depths (Fig. 3) and such that the maximum shear stress reaches the static yield strength

at a single point on the fault (Dalguer and Mai, 2008). Therefore, the location of the nucleation patch is predetermined by the location of the maximum in the random stress field. The initial shear stress was raised to 0.44% above the static failure stress inside the nucleation patch (diameter 3–6 km) in order to achieve stable sliding. Figure 3 (left panel) shows the initial normal stress σ_n and the initial shear stress τ_0 on the fault for rupture model B.

To emulate velocity strengthening in the shallow part of the crust, d_0 was increased from 0.2 m to 1.0 m in the top 4 km using a cosine taper. Similarly, μ_d was raised to a higher value than μ_s in the top 2 km of the crust, and tapered linearly between 2 km and 4 km depth (right panel in Fig. 3). Additionally, the shear stress τ_0 was tapered to zero at the free surface starting at 2-km depth using a ramp function. Due to the depth-dependent effective normal stress, both the static (τ_{cs}) and dynamic (τ_{cd}) failure stresses

$$\tau_{cs} = C + \mu_s \cdot \sigma'_n \quad \text{and} \quad \tau_{cd} = C + \mu_d \cdot \sigma'_n \quad (7)$$

increase continuously with depth. Therefore, the dynamic stress drop $\Delta\tau = \tau_0 - \tau_{cd}$ as well as the strength excess $\tau_{cs} - \tau_0$ also increase with depth (center panel in Fig. 3). The average stress drop in our four rupture models varies between 3.5 and 3.75 MPa.

The spontaneous rupture simulations were performed on a $63 \times 50 \times 40$ km³ mesh with a spatial discretization of 100 m. Figure 4 shows the final slip, rupture time, and peak slip rates on the fault obtained for the four rupture models. The slip rates in each of the four rupture models were multiplied with a factor near one to scale the final slip to a value consistent with an M_w 7.0 earthquake.

Both rupture models A and B nucleate in the lower left corner and propagate towards the right and towards the free surface, with the highest final slip and peak slip rates occurring on the right half of the fault. Rupture model C nucleates in the central part of the fault at approximately 10-km depth, while rupture model D has a deep, central hypocenter. In all rupture models, peak slip rates are highest in the deeper part of the fault, where they are up to 2 m·s⁻¹. Despite the emulated velocity strengthening in the shallow structure, slip rates of up to 1 m·s⁻¹ are reached close to the free surface for rupture models A and B. Rupture model C with its central, shallow hypocenter produces the lowest peak slip rates near the free surface, likely due to the minimal up-dip directivity for this model.

Rupture models A and B were mirrored laterally to analyze the effects of different rupture propagation directions on the resulting ground motions. Figure 1 shows the hypocenter locations after the planar rupture models were mapped onto the irregular fault geometry, with rupture models A' and B' referring to the laterally mirrored rupture models. The distribution of hypocenters was chosen to represent spots where a future M 7 earthquake is likely to nucleate. We placed five of our six hypocenter locations at 14- to 16-km depth below the surface, as normal-faulting earthquakes tend to nucleate near

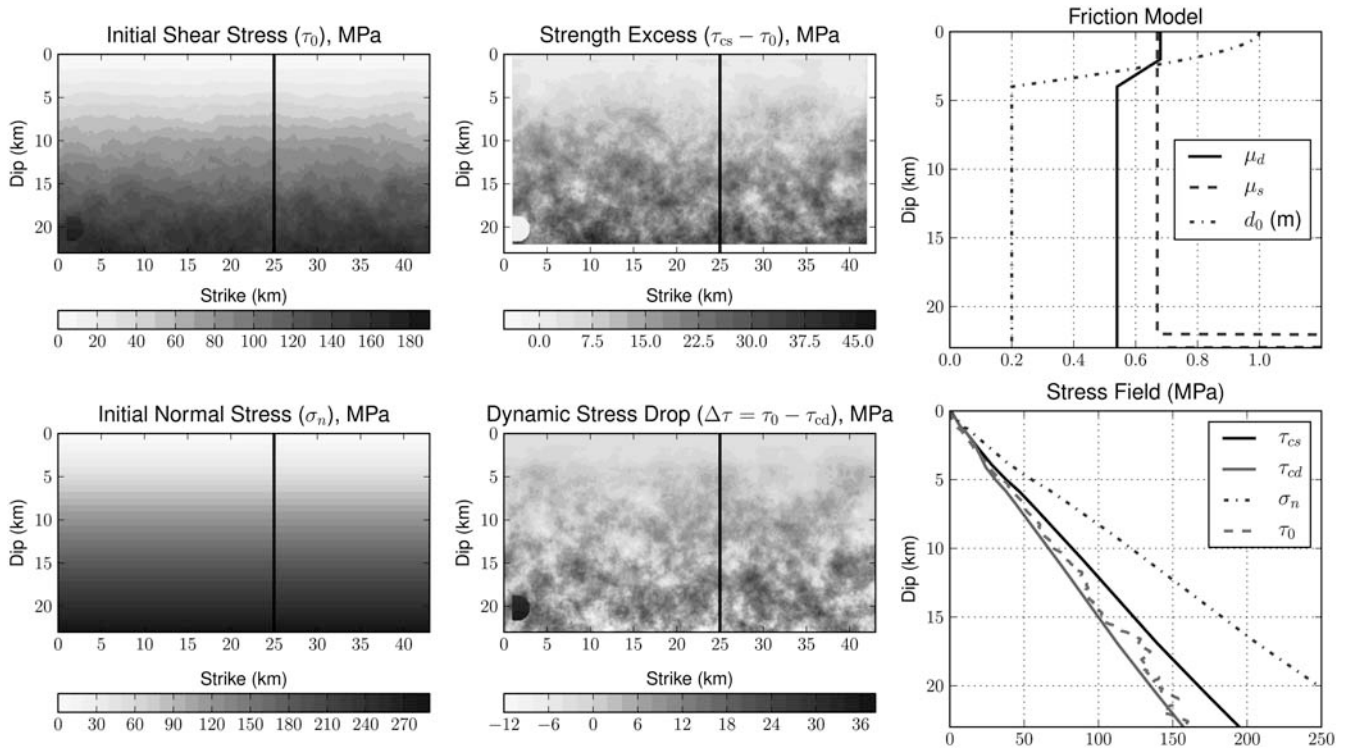


Figure 3. Distribution of dynamic rupture parameters on the fault for rupture model B. Left: Initial shear stress τ_0 and normal stress σ_n . Center: Strength excess $\tau_{cs} - \tau_0$ and dynamic stress drop $\Delta\tau = \tau_0 - \tau_{cd}$. Upper right: Static and dynamic coefficients of friction (μ_s and μ_d , respectively) and critical slip distance d_0 as a function of depth. Lower right: Static and dynamic failure stress (τ_{cs} and τ_{cd}), initial normal stress σ_n , and initial shear stress τ_0 as a function of depth at 25 km along-strike distance.

the brittle-ductile transition zone and then propagate upwards (e.g., [Smith and Arabasz, 1991](#); [Mai et al., 2005](#)). To analyze the influence of hypocenter depth on ground motions, we included scenario C, which nucleates at an intermediate depth of 7 km below the surface. [Bruhn et al. \(1992\)](#) proposed two potential sites for rupture initiation, both of which they interpreted as nonconservative slip barriers (in the sense that the slip vector changes across the barrier), one at the southern end of the WFSLC, where there is a sharp bend in the fault, and the other near the center of the WFSLC, where there is a left step in the mapped surface trace and an intersection with an older branch of the fault. We also considered hypocenters along the part of the WFSLC north of the downtown SLC tear fault, as [Bruhn et al. \(1992\)](#) interpreted this area as a third nonconservative barrier. Therefore, our ensemble of rupture scenarios includes models A and B initiating near the northern end, models A' and B' nucleating near the southern end, and models C and D starting near the central barrier (Fig. 1). Note that all of our initiation points are located at irregularities in the fault surface.

Our ensemble of four dynamic rupture models is based on a relatively small subset of possible parameterizations. For example, we selected a fractal model to generate the stochastic component of the initial stress distribution for all of the dynamic simulations. [Mai and Beroza \(2002\)](#) show that the fractal model describes the power spectrum of published slip distributions equally as well as von Karman and expo-

ponential autocorrelation functions, at least for faults with small aspect ratios. While there are many studies recommending self-similar, fractal, or von Karman stress distributions based on the spectral behavior of slip (e.g., [Mai and Beroza, 2002](#); [Guatteri et al., 2003](#); [Ripperger et al., 2007](#); [Schmedes et al., 2010](#)), we are not aware of any studies that recommend a specific distribution based directly on observed ground motions. [Ripperger et al. \(2008\)](#) suggest that the interevent variability of ground motion is dominated by the effects of differing hypocenter locations and that the details of the heterogeneous stress distribution are of lesser importance. In our study, the hypocenters are varied and selected from plausible nucleation points on the fault.

A further limitation is that all of our rupture models are based on a simple slip-weakening law (equation 6), which has been used extensively in both numerical and observational studies (e.g., [Andrews, 1976](#); [Madariaga et al., 1998](#); [Fukuyama et al., 2003](#); [Cruz-Atienza et al., 2009](#)). However, it is known that laboratory observations are better explained with a rate-and-state variable friction law (e.g., [Scholz, 1998](#)), which describes the dependency of the friction coefficient on slip velocity (i.e., velocity strengthening or velocity weakening). Many studies support the presence of a velocity-strengthening layer near the surface (e.g., [Day and Ely, 2002](#); [Somerville and Pitarka, 2006](#); [Dalguer et al., 2008](#); [Kaneko et al., 2008](#)). Because the slip-weakening friction model implemented in our dynamic rupture code does

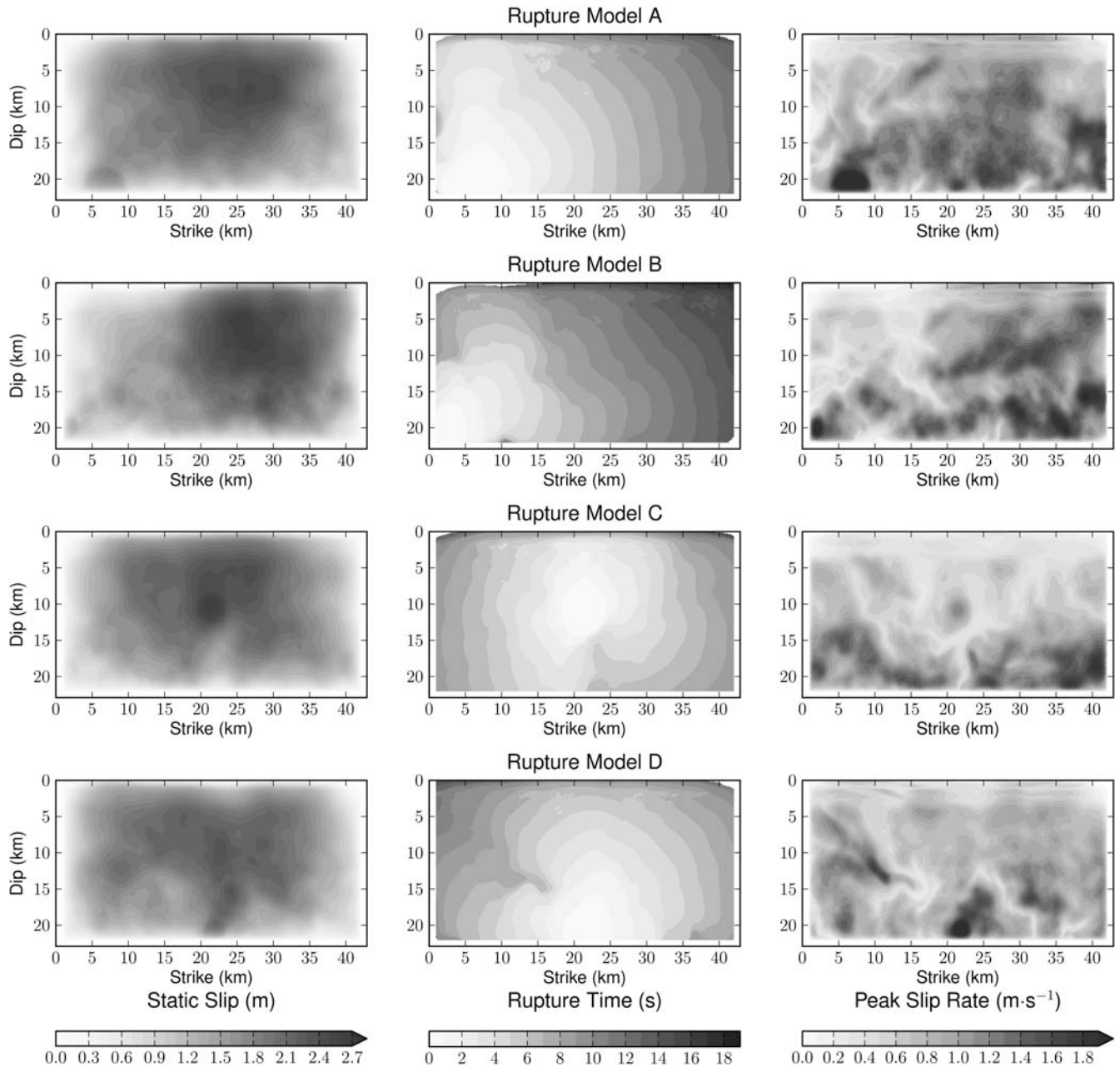


Figure 4. Static slip, rupture times, and peak slip rates obtained from the four rupture models.

not model rate-and-state friction directly, we have emulated the velocity-strengthening layer in the crust by adjusting μ_d and d_0 as described earlier in this section.

Kinematic Rupture Models

We generated six kinematic source models from the spontaneous rupture simulation results. While the wave-propagation simulations are performed with a grid step of 40 m, we discretized the WFSLC model on an 80-m grid to limit the size of the moment-rate files. For each subfault on the discretized fault model, the moment-rate time histories were computed using the following procedure:

1. We use the along-strike and downdip position (contour lines in Fig. 1) to find the corresponding location in the planar rupture model.
2. The slip-rate time histories for that location in the along-strike direction x_n and along-dip direction z_n (where the timestep $n = t_0 \dots t_n$) are extracted from the spontaneous rupture results using a 2D spline interpolation (Press *et al.*, 2007).
3. A third-order, one-pass Butterworth low-pass filter with a corner frequency of 1.2 Hz is applied to x_n and z_n . The slip-rate time histories are resampled to the desired temporal discretization Δt using a linear interpolation.
4. We define the along-dip slip direction as a unit vector \mathbf{U}_{\parallel} , which has an azimuth of 240° (Bruhn *et al.*, 1992) and is

parallel to the local surface of the irregular fault. \mathbf{U}_{\parallel} is multiplied by the slip rate z_n , to form the along-dip component \mathbf{S}_{\parallel}^n of the slip-rate time series.

5. We calculate the direction of unit vector \mathbf{U}_{\perp} , which is perpendicular to \mathbf{U}_{\parallel} and parallel to the local fault surface, pointing towards the strike direction. This vector is multiplied by x_n to form the along-strike component \mathbf{S}_{\perp}^n of the slip-rate time series.
6. We evaluate the time-dependent slip-rate vector $\mathbf{S}^n = \mathbf{S}_{\parallel}^n + \mathbf{S}_{\perp}^n$, and the slip-rate amplitude $|\mathbf{S}^n|$.
7. We calculate the local strike ϕ_f and local dip θ on the irregular fault. The rake λ_n is defined as the angle between \mathbf{S}^n and the strike direction. Therefore, λ_n is time-dependent, allowing for rake rotation.
8. We apply a ramp taper $k(\theta)$ in order to reduce slip on fault segments with unrealistically shallow dips for reasons explained in the paragraph following this list:

$$k(\theta) = \begin{cases} 0 & \text{if } \theta < 25^\circ \\ \frac{(\theta - 25^\circ)}{5^\circ} & \text{if } 25^\circ \leq \theta < 30^\circ \\ 1 & \text{if } \theta \geq 30^\circ \end{cases} \quad (8)$$

9. We compute the moment-rate tensor elements $T_{ij}^{(n)}$ from the strike ϕ_f , dip θ , and rake λ_n for each timestep n . The moment-rate tensor time series is scaled by the local shear modulus μ , the area of the subfault element A , and the slip-rate amplitude:

$$T_{ij}^{(n)} = |\mathbf{S}^n| \mu A k(\theta) (n_i \hat{d}_j^n + n_j \hat{d}_i^n), \quad (9)$$

where $\hat{\mathbf{n}}$ and $\hat{\mathbf{d}}$ are unit vectors oriented normal to the fault and along the slip direction, respectively.

The taper $k(\theta)$ was introduced to eliminate slip on fault nodes where the dip is unintentionally low, as is the case for the shallow part of the stepover connection near Holladay (Fig. 1). Bruhn *et al.* (1992) assigned a dip of 30° to this section using geometric modeling, which is the smallest dip anywhere in their WFSLC model. In the fault geometry provided by the WFCVM, the local dip in this area is even smaller ($< 25^\circ$) for a few of the shallowest subfaults. Because the geometry of this fault segment is poorly constrained, normal faults generally steepen near the surface rather than flattening out and there are no large fault scarps at the surface along the stepover; we decided to eliminate slip on the shallow part of the Holladay stepover connection using the dip-dependent taper. A second taper was applied to subfaults located inside a circular area of 3-km radius around the hypocenter to reduce artifacts produced by the artificial initiation of the rupture inside the nucleation patch.

The shear-modulus μ used to compute the moment rate in step (9) differs, in general, from the shear-modulus in the 1D model employed for the spontaneous rupture simulation. Consequently, the total seismic moment of the kinematic source deviates from the moment of the dynamic rupture models. To correct for this difference, the ground motions

obtained from the wave propagation simulations are multiplied with a correction factor to obtain the target magnitude M_w 7.0.

Ground Motions from M 7 Scenario Earthquakes

We simulated the wave propagation resulting from the six kinematic sources with the optimized, parallel AWP-ODC program (Cui *et al.*, 2010), which is based on the 3D velocity-stress staggered-grid FD code developed by Olsen (1994). Table 1 lists the key parameters used for the FD simulations. With a minimum shear-wave velocity $\min(v_s)$ of $200 \text{ m}\cdot\text{s}^{-1}$ and a grid step Δh of 40 m, frequencies of up to 1.0 Hz can be modeled using at least five grid points per wavelength. Surface topography was not included in the wave propagation model. We used a coarse-grained implementation of the memory variables for a constant- Q solid (Day and Bradley, 2001) and Q -velocity relations from Brocher (2006). 3D FD synthetic seismograms generated using this Q model and the WFCVM provide a satisfactory fit to data for a small earthquake below the Salt Lake Valley in the frequency range 0.5–1.0 Hz (Magistrale *et al.*, 2008).

Figure 5 shows snapshots of the east–west component of the ground velocity for rupture model B', which nucleates in the southern part of the SLB. We can identify both the direct S wave, propagating from south to north with the rupture (snapshots at 10 and 15 s), as well as basin-edge-generated surface waves, with wavefronts roughly parallel to the basin boundary (20 to 25 s). The interference of these phases generates large amplitudes in the northern part of the SLB for this scenario, e.g., up to $2 \text{ m}\cdot\text{s}^{-1}$ in downtown SLC (station 2289) and up to $1.3 \text{ m}\cdot\text{s}^{-1}$ near SLC international airport (station 2287). An animated version of these ground velocity snapshots is available as an [e](#)lectronic supplement to this article (Movie S1).

Computation of Horizontal Spectral Accelerations

As our simulations are limited to frequencies below 1 Hz, we analyze the spatial distribution of resulting ground motions by computing spectral accelerations for periods of 2 s (2-s SAs) and 3 s (3-s SAs). To combine the response

Table 1
Key Parameters in FD Simulations of Wave Propagation

Model Dimensions	$1500 \times 1125 \times 750$ (1.3×10^9 nodes) 60 (north-south) \times 45 (east-west) \times 30 (vertical) km
Simulation Length	60 s (24,000 time steps)
Horizontal Discretization Δh	40 m
Temporal Discretization Δt	2.5×10^{-3} s
Minimum v_s	$200 \text{ m}\cdot\text{s}^{-1}$
Highest Frequency	1.0 Hz
Number of CPU Cores	1875
Wall-Clock Runtime	2.5 hr (NICS Kraken*)

*See [Data and Resources](#) section.

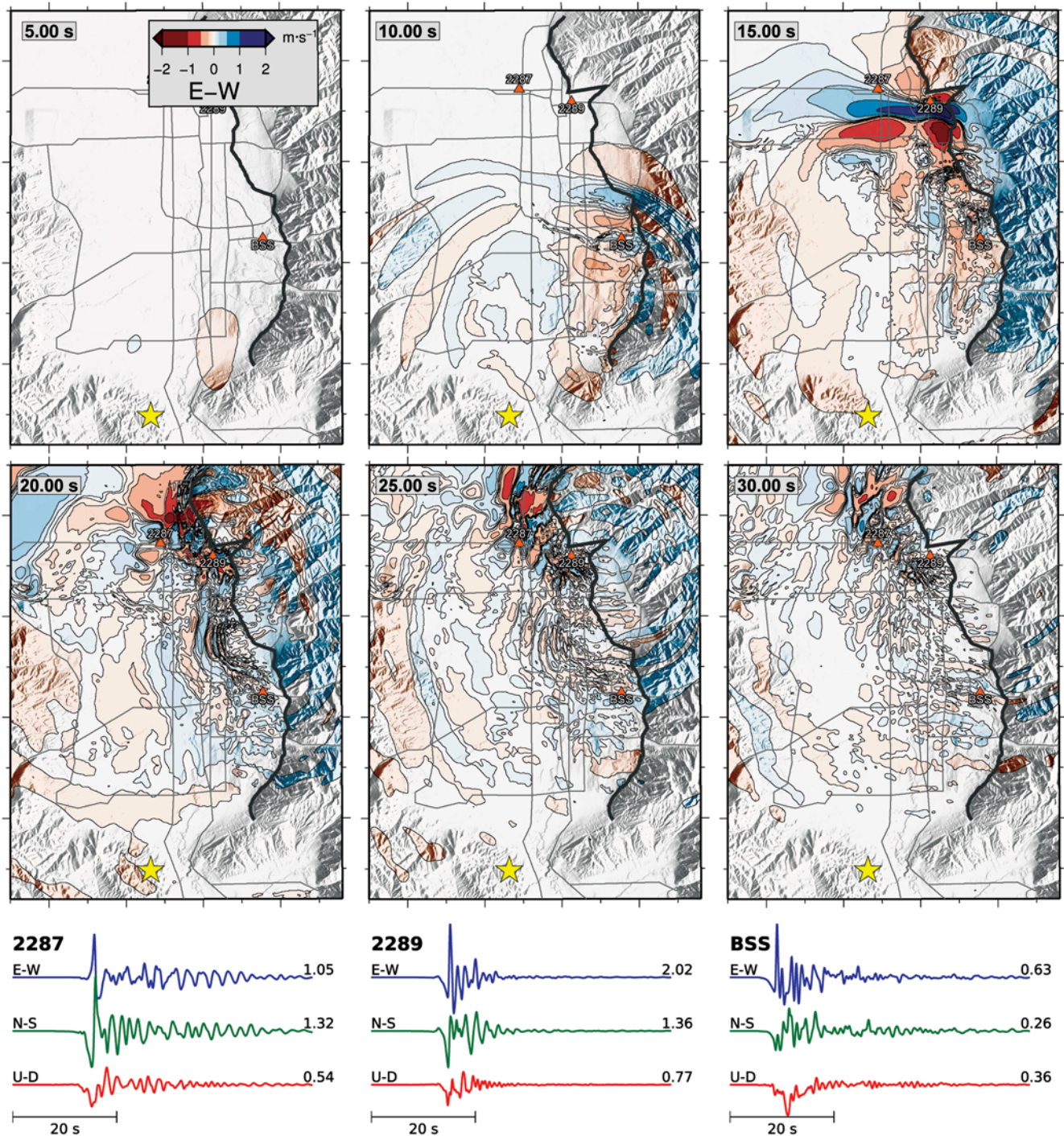


Figure 5. Snapshots of ground velocity along the east–west component for rupture model B', including seismograms at a few sites. The star shows the epicenter location. Numbers to the right of the seismograms indicate peak velocities ($\text{m}\cdot\text{s}^{-1}$). E-W, east–west; N-S, north–south; U-D, up–down.

spectra of the two horizontal components into a single measurement of ground shaking, we use the orientation-independent measure GMRotD50 defined by Boore *et al.* (2006). The GMRotD50 value is obtained by calculating the geometrical mean of the two horizontal-component spectral accelerations for a range of rotation angles θ , where $\theta = 0, \Delta\theta, \dots, \pi/2$ and $\Delta\theta \approx 1^\circ$, and taking the median. Because,

with this approach, the rotation angle θ corresponding to the median geometric mean depends on the period T of the response spectra, Boore *et al.* (2006) also define the measure GMRotI50, where the same rotation angle θ_{\min} is used for each period. θ_{\min} represents the rotation angle that minimizes extreme variations away from the median value over all periods. All next-generation attenuation relationships (NGAs)

use the GMRotI50 value. In our case, we are analyzing the spatial variability of the horizontal spectral acceleration for just a few selected periods between 1 and 10 s. Applications of the GMRotI50 value to recorded ground motions, however, typically use periods from 0.1 to 10 s. Therefore, we use the GMRotD50, rather than the GMRotI50 metrics, to compute rotation-independent spectral accelerations from both horizontal components.

Spectral Accelerations at Two Seconds (2-s SAs)

Figure 6 shows 2-s SAs for the horizontal components for all six scenarios. Spectral accelerations for scenario A, where the rupture nucleates in the northern part of the SLB, exceed $0.6g$ at many hanging-wall side locations, especially in the southern part of the SLB, where they exceed $0.8g$. Most of downtown SLC 2-s SAs remain below $0.5g$ for this scenario. Nearly everywhere on the footwall, 2-s SAs are below $0.3g$. The pattern is significantly different for scenario A', which is based on the same rupture model but mirrored laterally to make the rupture propagate from south to north. For this rupture direction, 2-s SAs in excess of $1g$ appear in the Cottonwood Heights area and near central SLC. For this scenario, we also observe values of more than $0.5g$ on the footwall side of the fault in the northern half of the SLB, where there are thin, stiff, unconsolidated sediments. This comparison suggests that rupture direction has a big impact on the ground motions for ruptures nucleating near either end of the fault segment.

Effects of rupture direction are even more pronounced for scenarios B and B'. 2-s SAs for scenario B, with the rupture nucleating near the northern end of the WFSLC, peak southeast of Cottonwood Heights, where they exceed $0.8g$. In the central SLC area, the 2-s SAs remain below $0.5g$ for scenario B. Scenario B', with the mirrored source model, however, produces stronger ground motions with 2-s SAs up to $1.4g$ near downtown SLC and on the hanging-wall side of the Warm Springs section.

The strong dependence of the 2-s SAs on rupture direction can be attributed, in part, to classical directivity. However, there are also other factors that contribute. The rupture direction effects can partly be traced back to the dynamic rupture models A and B (Fig. 4), with larger static slip and near-surface peak slip rates (more pronounced in model B than model A) at the end of the fault opposite the nucleation point. However, the generally higher 2-s SAs obtained for the two south-to-north rupturing scenarios A' and B' as compared to the two north-to-south rupturing scenarios A and B cannot be explained entirely as a source effect. This difference is likely influenced by the variation in depth and velocity of the unconsolidated sediments, which are deeper and lower velocity in the northern part of the SLB than in the southern part (Fig. 2; Olsen *et al.*, 1995; McDonald and Ashland, 2008). The depth of interface R_1 exceeds 300 m west of the Warm Springs segment and around downtown SLC (Fig. 2, right). In the southern SLB, R_1 is located

closer to the surface, mostly between 50- and 200-m depth. However, the depth of R_1 exceeds 200 m in the Cottonwood Heights area, just west of where we obtained the highest 2-s SAs for scenarios A and B.

Because periods near 2 s are especially important for buildings with approximately 20 stories, we have indicated the locations of high-rises (≥ 20 story buildings) in the downtown SLC area (white squares in Fig. 6). Even though high-rises are located just north of the hot spot southwest of the tear fault, they would still be subjected to spectral accelerations of more than $0.5g$ in scenarios A' and B'. Bruhn *et al.* (1992) suggested that the southern end of the WFSLC may have been the most common position for repetitive rupture initiation during previous earthquakes, based on the fault-segment geometry and on evidence that long-term deformation rates are highest at the southern barrier. Given this possibility, it is certainly important to note that a south-to-north rupture yields significantly higher 2-s SAs in downtown SLC than a north-to-south rupture. However, the geology in that area is rather complex, and the location of the tear fault is not well constrained. The use of a planar rupture model, which does not take the rupture dynamics caused by the irregular tear fault into account, represents another source of uncertainty for the simulated ground motion, especially in the downtown SLC area.

Rupture model C, with its central, shallow (7.2 km) hypocenter, yields much lower average 2-s SAs than the other five scenarios (Fig. 6). The highest values (2-s SAs of up to $0.6g$) for this scenario occur near downtown SLC and on the hanging-wall side of the WSF segment. These relatively low 2-s SAs reflect the generally low peak slip rates in the near-surface area obtained from the spontaneous rupture simulation for rupture model C (Fig. 4).

Like rupture model C, rupture model D features a central hypocenter but at a greater depth (14.5 km below the surface). 2-s SAs from this scenario exceed $0.5g$ in several areas on the hanging-wall side of the fault (Fig. 6), with values of up to $1.0g$ north of SLC. The spatial distribution of ground motions represents an intermediate case between scenarios A and B, rupturing southwards, and scenarios A' and B', rupturing towards the north. It is striking that the 2-s SAs are up to twice as large as those from scenario C, which has a more shallow hypocenter. This difference illustrates a secondary rupture-direction effect in the along-dip direction, with the deep hypocenter producing larger ground motions than the shallow hypocenter. This rupture direction effect is also evident in the spontaneous rupture simulation results, as peak slip rates in the uppermost 12 km and especially in the uppermost 4 km are larger for rupture model D than for rupture model C (Fig. 4).

Another striking observation that can be made from the simulated ground motions for all six scenarios is that the highest 2-s SAs are reached at some distance (1–2 km) from the surface rupture on the hanging-wall side, rather than directly at the rupture. This result is consistent with the peak ground velocity (PGV) maps for the Teton fault published by

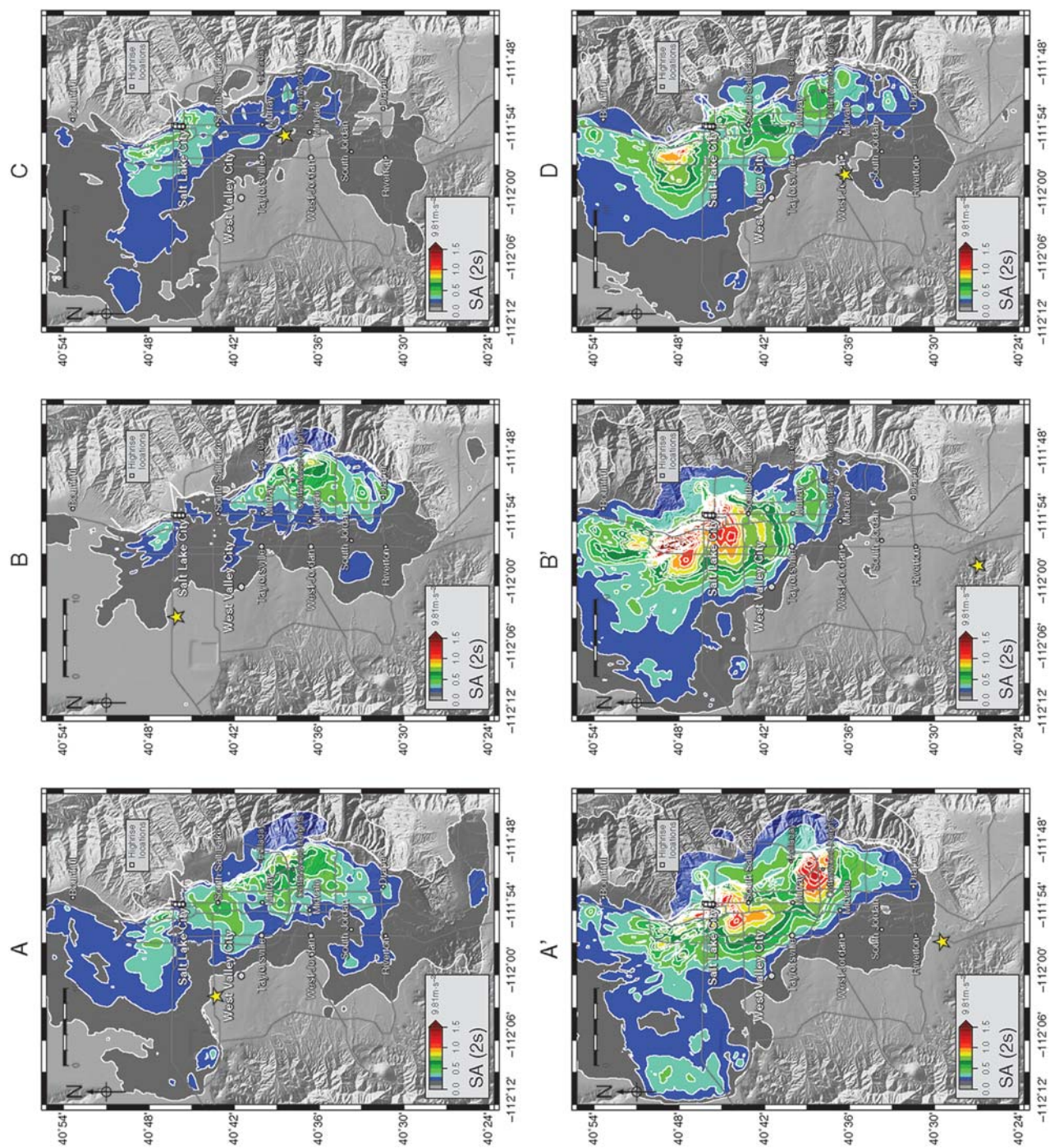


Figure 6. Rotation-independent horizontal 2-s SAs for all six scenarios.

O'Connell *et al.* (2007), where the highest PGVs occurred at distances of 1–4 km from the surface trace of the fault, also on the hanging-wall side.

Average 2-s SAs and 3-s SAs

Figure 7 (top) shows the geometric mean of the 2-s SAs and the standard deviation σ from all six scenarios. The average 2-s SAs exceed $0.3g$ within a 5- to 10-km-wide zone on the hanging-wall side of the fault and reach up to $0.6g$ close to downtown SLC and west of the Warm Springs section, as

well as in the Cottonwood Heights area in the southern SLB. This distribution correlates partly with the depth to the R_1 interface (Fig. 2, left). The large average 2-s SAs in the northern SLB are due to the high values obtained from scenarios A' and B', which is reflected in the relatively large standard deviation for downtown SLC and the area west of the Warm Springs segment. The southern patch of high average 2-s SAs exhibits rather large accelerations in all of the six scenarios, and is characterized by a lower standard deviation. Two areas with large mean 2-s SAs are located southwest of a stepover:

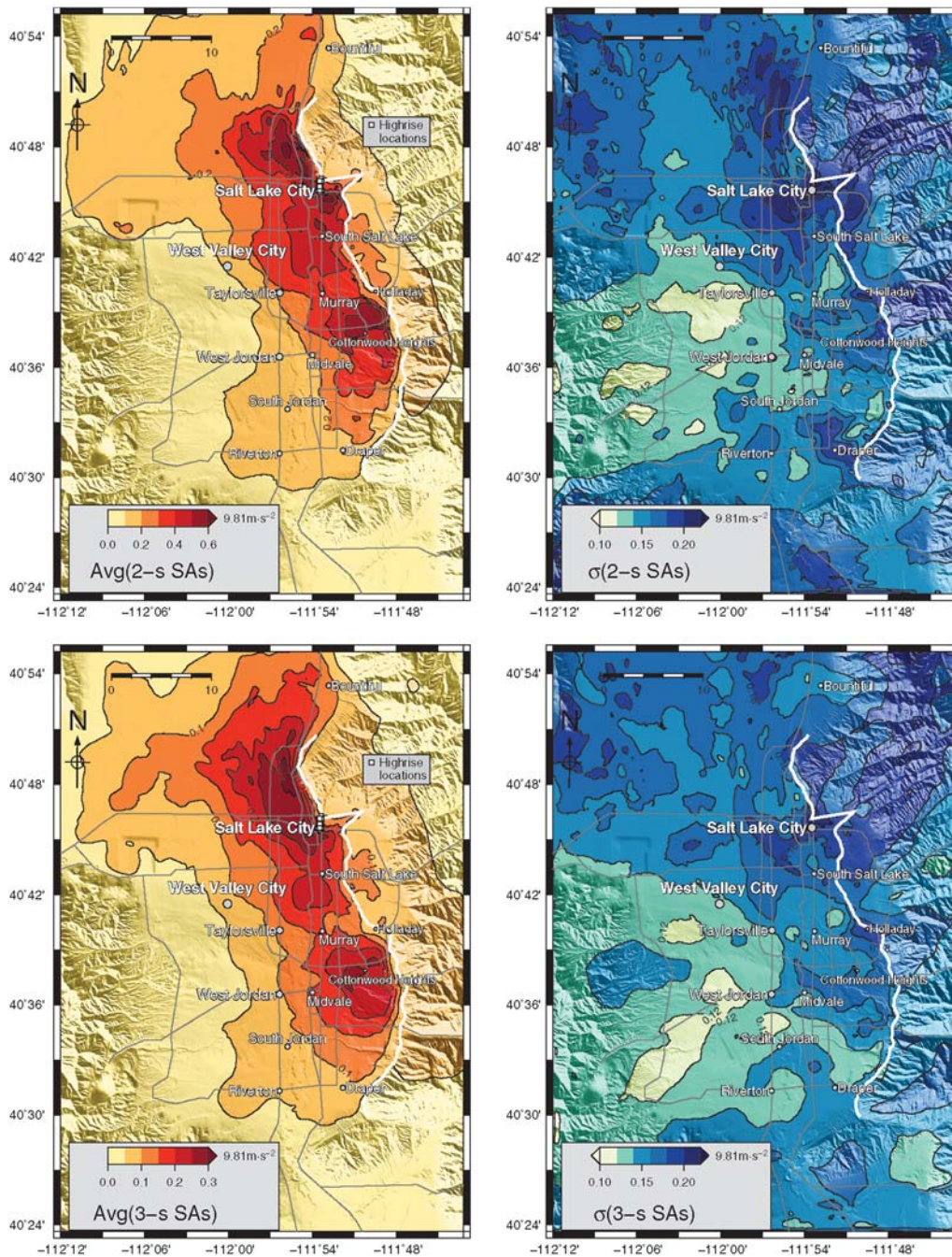


Figure 7. Geometric mean of 2-s SAs and 3-s SAs (left) and geometric standard deviation σ (right) from the six scenarios. Note the different scale for the mean 2-s SAs compared to Figure 6.

the small area southeast of downtown SLC, located south of the tear fault, and the Cottonwood Heights area southwest of the Holladay stepover. This result suggests that focusing effects caused by the concavely shaped fault geometry might contribute to the high average 2-s SAs in these areas (see Olsen and Schuster, 1994).

Average 3-s SAs show a very similar spatial distribution, but values do not exceed $0.35g$ for this period. Maps with 3-s SAs from individual scenarios are available as an [electronic supplement](#) to this paper (Fig. S1).

Comparison to Next-Generation Attenuation Models

We evaluate the simulated ground motions by comparing the mean SAs from all six scenarios with values predicted by NGA models. We chose four of these recent attenuation relations: Boore and Atkinson (2008), Campbell and Bozorgnia (2008), Abrahamson and Silva (2008), and Chiou and Youngs (2008). For the remainder of this text, we will refer to these relations as BA08, CB08, AS08, and CY08, respectively. These four NGA relations use different source distance definitions. BA08 use only the Joyner–Boore distance, R_{JB} , which is defined as the closest distance to the surface projection of the fault rupture. In the case of the normal-faulting WFSLC, R_{JB} is zero for a large area inside the SLB (left panel in Fig. 8). CB08, AS08, and CY08 use both R_{JB} and the closest distance to the rupture surface, R_{Rup} .

Additionally, AS08 and CY08 require R_x , which is defined as the shortest distance from a site to the top of the rupture (extended to infinity in both directions), measured perpendicular to the fault strike.

All of the NGA models use the average shear-wave velocity in the top 30 m, V_{S30} . For the comparison, we focus on the ground motions on the softest sediments on the hanging-wall side, where the simulations yield the strongest ground motion. We chose all sites in the computational area where V_{S30} is between 200 and $300 \text{ m}\cdot\text{s}^{-1}$ in the velocity model and evaluated the NGA predictions for $V_{S30} = 250 \text{ m}\cdot\text{s}^{-1}$. We obtained V_{S30} in the computational model by interpolating from the value at the free surface, $v_s^{k=0}$, and at the first node 40 m below the surface, $v_s^{k=1}$. Highlighted patches in Figure 8 (left) show the areas that were used for the comparison with Boore and Atkinson (2008), and contour lines show R_{JB} .

Spectral observations from the simulations were binned into 20 distance ranges, spaced logarithmically between 1 and 20 km. The bin centered at $R_{JB} = 1$ km includes 1.2×10^6 grid points with $0 \leq R_{JB} \leq 1$ km and represents a larger sample size than the remaining bins, which contain between 1.4×10^4 and 2.3×10^5 grid points (Fig. 8). Geometric means for $R_{JB} \leq 1$ km exceed the values predicted by the BA08 relation by $\sim 25\%$ for 3-s SAs and by $\sim 40\%$ for 2-s SAs. At R_{JB} distances of 1 to 15 km, all of the 2-s and 3-s

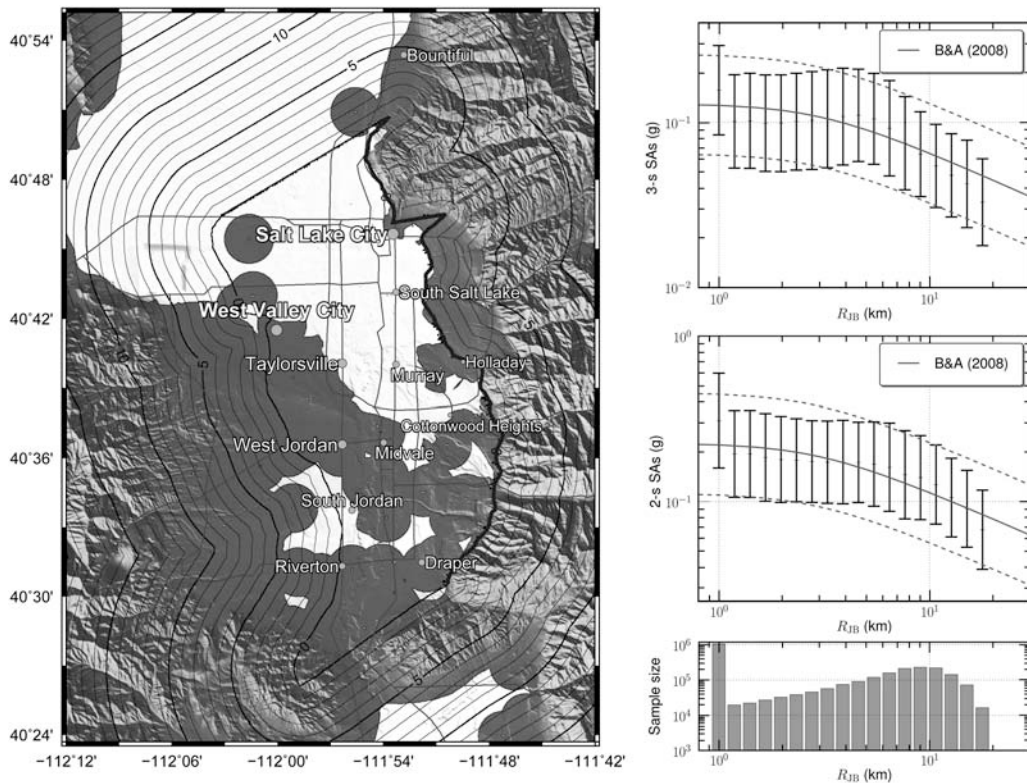


Figure 8. Left: Joyner–Boore distance R_{JB} (black contours) and areas used for comparison with BA08, where $200 \text{ m}\cdot\text{s}^{-1} \leq V_{S30} \leq 300 \text{ m}\cdot\text{s}^{-1}$ (highlighted areas). Right: Geometric mean of 3-s SAs and 2-s SAs obtained from the ensemble of rupture models including the geometric standard deviation (error bars). Solid lines show the predictions according to BA08, and dashed lines show the geometric standard deviation. The histogram on the lower right shows the number of samples in each distance bin.

simulated mean SAs are within 25% of the BA08 predictions. It is noteworthy that the simulated mean 3-s SAs are higher for R_{JB} s of 4 to 5.5 km than for $R_{JB} = 2$ km. This observation could be explained by the relatively large average 3-s SAs 5 km northwest of the northwest edge of the rupture (Fig. 7), where most grid points with $R_{JB} \approx 5$ km in the area of comparison are located.

In general, the agreement between the mean simulated 3-s SAs and 2-s SAs and the values predicted by the equation of BA08 is very favorable. The geometric standard deviation of 2-s SAs and 3-s SAs from the simulated ground motions is also quite close to the predicted values. This agreement suggests that our ensemble of six FD simulations adequately represents the variability in ground motions. However, we note that using the Joyner–Boore distance alone can be problematic for the WFSLC because $R_{JB} = 0$ for a large area that shows a significant variability in the simulated ground motions.

For this reason, we performed a similar comparison for the area with $R_{JB} = 0$ using the ground-motion prediction equations by CB08, AS08, and CY08 as a function of R_{Rup} . In order to remove the dependency of AS08 and CY08 on R_x for plotting purposes, we followed the OpenSHA (2010) approach by setting

$$\frac{R_{Rup} - R_x}{R_{Rup}} \quad (10)$$

equal to its average value within the area of interest. Inside the area considered for the comparison ($R_{JB} = 0$,

$200 \text{ m}\cdot\text{s}^{-1} \leq V_{s30} \leq 300 \text{ m}\cdot\text{s}^{-1}$), this normalized difference between R_{Rup} and R_x (equation 10) averages to -0.40 ± 0.23 (standard deviation). It is negative as R_x is defined as positive on the hanging-wall side. Additionally, CB08 requires the parameter $Z_{2.5}$, which is defined as the depth where the shear-wave velocity reaches $2500 \text{ m}\cdot\text{s}^{-1}$; we chose $Z_{2.5} = 2.71$ km as an average value estimated from the WFSLC. AS08 and CY08 use the depth Z_1 where v_s reaches $1000 \text{ m}\cdot\text{s}^{-1}$. We evaluated AS08 and CY08 using the average of Z_1 in the selected area (highlighted patches in Fig. 9), which is 389 ± 95.4 m (standard deviation).

For rupture distances below 4 km, the average simulated 3-s SAs and 2-s SAs are generally within the range of values spanned by the CB08, AS08, and CY08 predictions and well as within one standard deviation of all three models. For larger rupture distances, the average simulated SAs fall below the values predicted by all three NGA models. At $R_{Rup} \sim 10$ km, the simulated 3-s SAs and 2-s SAs are about one standard deviation below the NGA predictions. The saturation of the simulated 3-s SAs and 2-s SAs at small rupture distances is in agreement with the NGA curves. The highest simulated average 3-s SAs are reached at rupture distances between 1.2 and 2.7 km, while the largest average 2-s SAs are encountered at R_{Rup} between 1.15 and 1.5 km. It is important to keep in mind that, as mentioned earlier, the data set used to determine the attenuation relations provides no direct constraints for $M 7$ normal-faulting earthquakes.

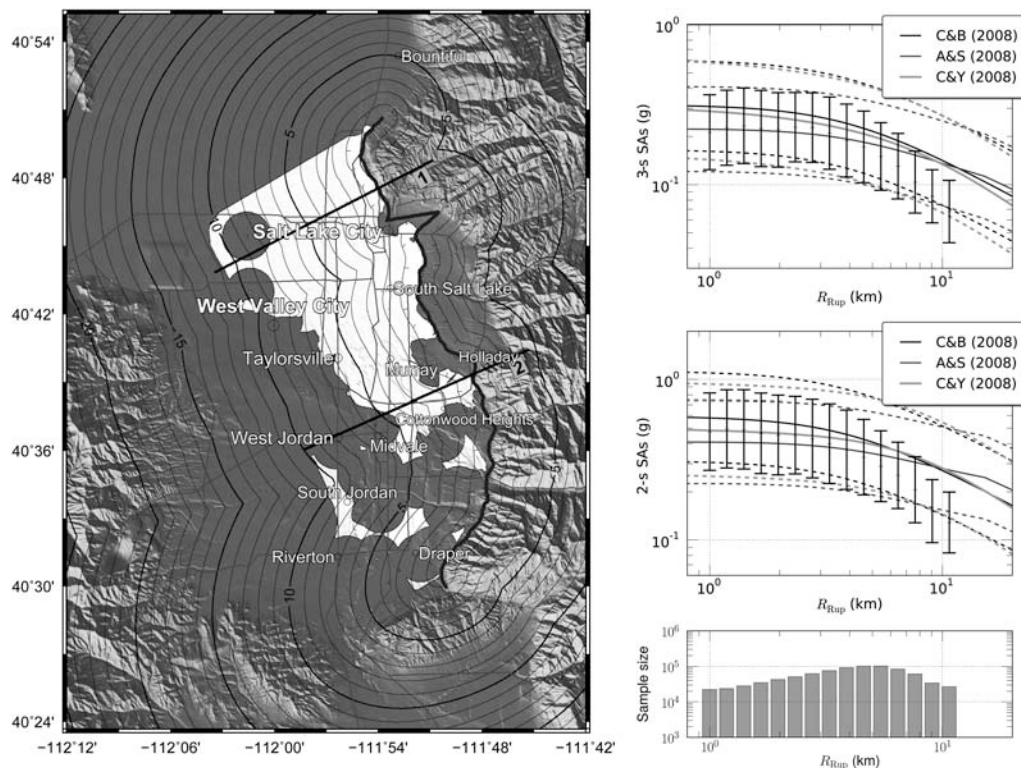


Figure 9. Same as Figure 8, but showing comparisons to CB08, AS08, and CY08 as a function of R_{Rup} (black contours on the map) for $R_{JB} = 0$. The straight black lines mark the locations of the cross sections shown in Figure 11.

Simulated average ground motions on bedrock sites on the footwall tend to be much lower than those on hanging-wall sediments (Fig. 7). To see if the NGA models predict a similar trend, we performed a comparison for all the sites on the footwall with V_{S30} above $1000 \text{ m}\cdot\text{s}^{-1}$ inside the computational domain (left panel in Fig. 10), excluding the absorbing boundaries. We evaluated the four NGA models using the average V_{S30} of $1443 \text{ m}\cdot\text{s}^{-1}$ inside the area of comparison. Because $R_{JB} = R_{Rup}$ on the footwall side, the predictions of BA08 can be directly compared with those of the other three relations. Additionally, we assumed that $R_x = R_{Rup}$ on the footwall to simplify the comparisons with AS08 and CY08.

The central panels in Figure 10 compare simulated 3-s SAs and 2-s SAs with the BA08 and CB08 predictions. The simulated 3-s SAs agree well with the values from CB08 for rupture distances above 3 km. For smaller rupture distances, the simulated values are up to 30% lower than CB08 but still within one standard deviation. 3-s SAs predicted by BA08 are generally one standard deviation lower than the simulations. The comparison for 2-s SAs yields very similar results. AS08 and CY08 predict similar ground motions as CB08, and compare favorably with the simulated 3-s SAs and 2-s SAs (right panels in Fig. 10). We note that the simulated SAs tend to be below the NGA relations for $R_{Rup} < 4 \text{ km}$ and $R_{Rup} < 8 \text{ km}$ for 3-s SAs and 2-s SAs, respectively. Simulated SAs experience a sharp drop for $R_{Rup} \approx 20 \text{ km}$, which we attribute to the much smaller sample size in the last distance bin (bottom right panel in Fig. 10).

Discussion

Figure 11 shows average spectral acceleration ratios (SARs) as a function of horizontal distance from the top of

the rupture, R_x , along two cross sections oriented perpendicular to the fault (Fig. 9). We computed the SARs by dividing the SA along the cross section by the value obtained on a reference site on the footwall. SARs are shown for five different frequencies from 0.2 to 1.0 Hz. Along cross section 1, the SARs peak near 2.5 km from the surface rupture for 0.2 Hz, but they peak between 1.0 and 2.5 km distance for other frequencies. The SARs along cross section 2 peak between 1 and 5 km distance from the surface rupture, with the maximum SARs occurring closer to the fault for shorter wavelengths. This wavelength-dependent amplification pattern is consistent with the basin-edge effect, which is caused by interference between edge-generated surface waves and the direct S wave (e.g., Kawase, 1996; Pitarka *et al.*, 1998). Surface-wave dispersion results in longer wavelengths traveling faster than shorter wavelengths, shifting the location of interference with the direct S wave further away from the fault. Hallier *et al.* (2008), for example, performed 2D simulations for a basin bounded by a 68° -dipping normal fault and observed that the maximum amplification occurs further away from the fault for the low-frequency band (0–2 Hz) than for the high-frequency band (2–4 Hz). Figure 11 suggests that the peaks in 2-s SAs and 3-s SAs between 1 and 5 km from the surface rupture and their drop-off near the rupture can be explained by the basin-edge effect.

The approximation of velocity strengthening in the dynamic rupture models provides an alternative explanation for the occurrence of peak SAs at a distance from the fault. As a consequence of forcing $\mu_d > \mu_s$ near the free surface, peak slip rates tend to be lower in the uppermost 4 km of the fault than at greater depth (Fig. 4). Therefore, the possibility cannot be excluded that the drop-off in simulated SAs near

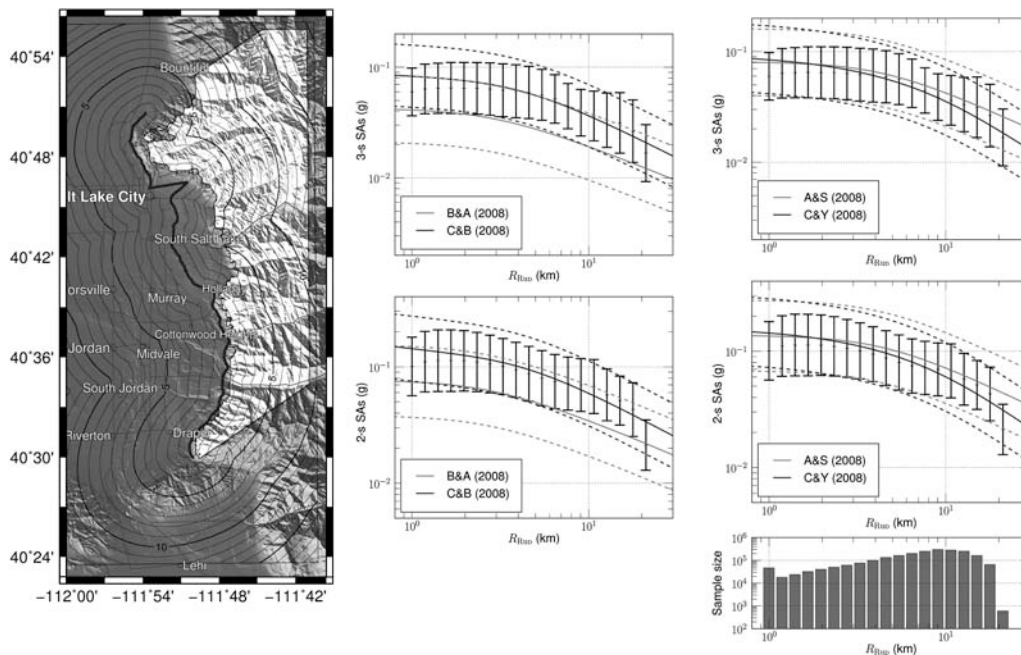


Figure 10. Same as Figures 8 and 9, but showing comparisons with the four NGA models for bedrock sites on the footwall.

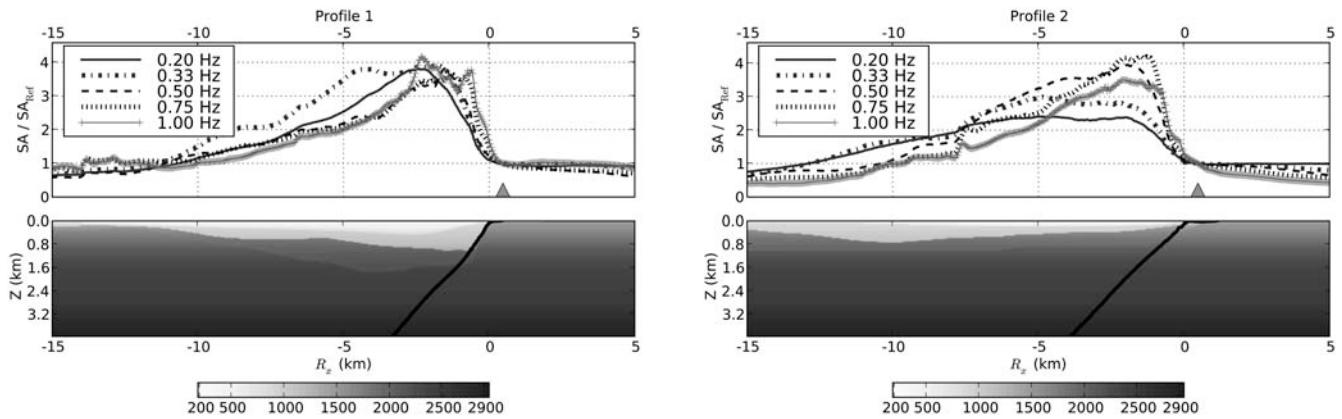


Figure 11. Average sediment-to-bedrock spectral acceleration ratios for five different frequencies along the two cross sections indicated in Figure 9. The triangle shows the location of the bedrock site used for the normalization.

the fault is caused, at least in part, by the emulated velocity strengthening.

Aagaard *et al.* (2004) studied rupture directivity effects for strike-slip earthquakes on vertical faults and for thrust earthquakes on shallow dipping faults. They concluded that strong directivity effects exist only if the rupture propagates parallel to the direction of the fault-slip vector. In the case of dip-slip rupture, this conclusion implies that a moderate directivity effect exists in the up-dip direction for deep hypocenters, while directivity effects are minimal in the along-strike direction for unilateral ruptures. The along-strike rupture direction effects that are obvious from the differences between scenarios A and A' and between scenarios B and B' seem to contradict the findings of Aagaard *et al.* (2004). However, the wave-propagation simulations presented in this paper were performed for a velocity mesh with strong lateral heterogeneities, while the material properties varied only with depth in the simulations of Aagaard *et al.* (2004). It is obvious that Love and Rayleigh waves generated at the lateral discontinuity between the hanging-wall and the footwall side of the surface rupture contribute to the strong ground motion on the low-velocity sediments of the SLB. As the rupture propagates in the along-strike direction, these surface waves are continuously generated at the basin-edge, interfering with each other to generate a directivity pattern. The absence of lateral material heterogeneities near the free surface may explain why Aagaard *et al.* (2004) did not report a strong directivity effect in the along-strike direction for the thrust fault.

Conclusions

We performed numerical simulations for six $M 7$ scenario earthquakes on the WFSLC with the FD method for frequencies up to 1 Hz. These six scenarios are based on four rupture models obtained from simulations of spontaneous rupture on a planar, vertical normal fault with depth-dependent normal stress. We assess our results using horizontal spectral accelerations at 3 s and 2 s computed from the simulated ground motions. Significant along-strike rupture direction effects

occur for events nucleating near either end of the segment. Events A' and B', which nucleate near the southern end, generate much larger ground motions (2-s SAs of up to $1.4g$) in the downtown SLC area than events A and B, which initiate near the northern end (2-s SAs $< 0.5g$). The fact that identical rupture models generate such different ground-motion patterns when mirrored laterally is probably the result of a combination of source directivity and site effects. These results are especially significant because the southern barrier was identified as the most likely initiation point during past earthquakes (Bruhn *et al.* 1992). Events C and D, which nucleate near the central barrier, generate intermediate ground motions (2-s SAs up to $\sim 1g$) north of SLC and up to $0.6g$ in the downtown SLC area. Results from these two scenarios suggest that a rupture direction effect is also present along the dip direction, with the deeper hypocenter generating larger ground motions than the shallower hypocenter.

Average SAs from the six scenarios reach or exceed $0.3g$ at 3 s and $0.6g$ at 2 s on the deep sediments west of the Warm Springs section, near downtown SLC and near the Cottonwood Heights area. We find that the simulated ground motions are generally consistent with four recent NGA relations. Average SAs on the hanging wall exceed the prediction of BA08 by $\sim 25\%$ for 3-s SAs and $\sim 40\%$ for 2-s SAs where $R_{JB} \leq 1$ km, but they are consistent with predictions by CB08, AS08, and CY08 for $R_{JB} = 0$ and $R_{Rup} < 4$ km.

The scenario earthquakes presented in this text constitute the basis for a follow-up study in which broadband synthetics are derived by combining the low-frequency (< 1 Hz) ground motions with high-frequency scattering operators. These broadband (0–10 Hz) synthetics are used to produce SA maps at frequencies above 1 Hz and serve as input signals to simulate nonlinear soil behavior during future $M 7$ earthquakes in the SLB.

Data and Resources

The Wasatch Front Community Velocity model (WFCVM) is available from the Utah Geological Survey

(http://geology.utah.gov/ghp/consultants/geophysical_data/cvm.htm, last accessed May 2011). Maps presented in this text were made using the Generic Mapping Tools version 4.5.0 (<http://www.soest.hawaii.edu/gmt>, last accessed May 2011) by Wessel and Smith (1998). 3D graphics and animations were created with the Visualization toolkit (<http://www.vtk.org>, last accessed May 2011) by Schroeder et al. (2006). 2D plots were created with the Matplotlib (<http://matplotlib.sourceforge.net>, last accessed May 2011) graphics package for Python (Hunter, 2007). We used the OpenSHA attenuation relationship plotter (<http://www.opensha.org>, last accessed May 2011) and the MATLAB scripts from the Baker research group (<http://www.stanford.edu/~bakerjw/attenuation.html>, last accessed May 2011) to generate attenuation curves.

Simulations of wave propagation and spontaneous rupture were performed on the Teragrid resources National Institute for Computational Sciences (NICS) Kraken and Texas Advanced Computing Center (TACC) Ranger under an NSF allocation. The generation of the kinematic source from the spontaneous-rupture results requires considerable amount of computational time due to the spatial and temporal interpolations and the volume of the data. We implemented the moment-rate generation code as a parallel application using the MPI-2 library, reducing the wall-clock time to less than 3 hr per scenario using 36 cores on NICS Kraken. This tool directly generates source partitions suitable for parallel input/output in the wave propagation code.

Acknowledgments

The authors are grateful to Arthur Rodgers and Robert Graves for their detailed reviews that helped to improve the manuscript. We wish to thank Luis A. Dalguer for his valuable help in generating the depth-dependent shear-stress distribution for the spontaneous rupture models. Yifeng Cui and Kwangoon Lee from SDSC helped to run the FD simulations. This research was supported by a fellowship for prospective researchers (to D. Roten) from the Swiss National Science Foundation (PBEZ22-117264) and by the U.S. Geological Survey (USGS), Department of the Interior, under USGS award numbers 06HQGR0205 and 06HQGR0206.

References

- Aagaard, B., J. Hall, and T. Heaton (2004). Effects of fault dip and slip rake angles on near-source ground motions: Why rupture directivity was minimal in the 1999 Chi-Chi, Taiwan, earthquake, *Bull. Seismol. Soc. Am.* **94**, no. 1, 155–170.
- Abrahamson, N., and W. Silva (2008). Summary of the Abrahamson & Silva NGA ground-motion relations, *Earthq. Spectra* **24**, no. 1, 67–97.
- Adan, S., and K. Rollins (1993). Damage potential index mapping for Salt Lake Valley, Utah, *Utah Geol. Surv. Misc. Pub. 93-4*, 64 pp.
- Andrews, D. (1976). Rupture propagation with finite stress in antiplane strain, *J. Geophys. Res.* **81**, no. 20, 3575–3582.
- Bard, P.-Y., and M. Bouchon (1980a). The seismic response of sediment-filled valleys, Part 1: The case of incident *SH* waves, *Bull. Seismol. Soc. Am.* **70**, no. 4, 1263–1286.
- Bard, P.-Y., and M. Bouchon (1980b). The seismic response of sediment-filled valleys, Part 2: The case of incident *P* and *SH* waves, *Bull. Seismol. Soc. Am.* **70**, no. 5, 1921–1941.
- Benz, H., and R. Smith (1988). Elastic-wave propagation and site amplification in the Salt Lake valley, Utah, from simulated normal faulting earthquakes, *Bull. Seismol. Soc. Am.* **78**, no. 6, 1851–1874.
- Black, B., W. Lund, and B. Mayes (1995). Large earthquakes on the Salt Lake City segment of the Wasatch fault zone—summary of new information from the South Fork Dry Creek site, Salt Lake County, Utah, in *Environmental and Engineering Geology of the Wasatch Front Region: 1995 Symposium and Field Conference*, W. R. Lund (Editor), Utah Geol. Assoc. Publ. 24, Utah Geological Association, Salt Lake City, pp. 11–30.
- Boore, D., J. Watson-Lamprey, and N. Abrahamson (2006). Orientation-independent measures of ground motion, *Bull. Seismol. Soc. Am.* **96**, no. 4A, 1502–1511.
- Boore, D. M., and G. M. Atkinson (2008). Ground-motion prediction equations for the average horizontal component of PGA, PGV, and 5%-damped PSA at spectral periods between 0.01 s and 10.0 s, *Earthq. Spectra* **24**, no. 1, 99–138.
- Brocher, T. (2006). Key elements of regional seismic velocity models for ground motion simulations, in *Proc. of Int. Workshop on Long-Period Ground Motion Simulations and Velocity Structures*, Tokyo, Japan, 14–15 Nov.
- Bruhn, R., P. Gibling, W. Houghton, and W. Parry (1992). Structure of the Salt Lake segment, Wasatch normal fault zone: Implications for rupture propagation during normal faulting, in *Assessment of Regional Earthquake Hazards and Risk Along the Wasatch Front, Utah*, U. S. Geol. Surv. Prof. Pap. 1500-A-J, pp. H1–H25.
- Campbell, K. W., and Y. Bozorgnia (2008). NGA ground motion model for the geometric mean horizontal component of PGA, PGV, PGD and 5% damped linear elastic response spectra for periods ranging from 0.01 to 10 s, *Earthq. Spectra* **24**, no. 1, 139–171.
- Chiou, B., and R. Youngs (2008). An NGA model for the average horizontal component of peak ground motion and response spectra, *Earthq. Spectra* **24**, no. 1, 173–215.
- Chiou, B., R. Darragh, N. Gregor, and W. Silva (2008). NGA strong-motion database, *Earthq. Spectra* **24**, no. 1, 23–44.
- Cornou, C., P.-Y. Bard, and M. Dietrich (2003). Contribution of dense array analysis to the identification and quantification of basin-edge-induced waves, Part II: Application to Grenoble basin (French Alps), *Bull. Seismol. Soc. Am.* **93**, 2624–2648.
- Cruz-Atienza, V., K. Olsen, and L. Dalguer (2009). Estimation of the breakdown slip from strong-motion seismograms: Insights from numerical experiments, *Bull. Seismol. Soc. Am.* **99**, no. 6, 3454.
- Cui, Y., K. Olsen, K. Lee, J. Zhou, P. Small, D. Roten, G. Ely, D. Panda, A. Chourasia, J. Levesque, S. Day, and P. Maechling (2010). Scalable earthquake simulation on petascale supercomputers, in *Proc. of SC10*, New Orleans, Louisiana, 13–19 November.
- Dalguer, L., and S. Day (2007). Staggered-grid split-node method for spontaneous rupture simulation, *J. Geophys. Res.* **112**, B02302, doi: [10.1029/2006JB004467](https://doi.org/10.1029/2006JB004467).
- Dalguer, L. A., and M. Mai (2008). Implications of style-of-faulting and loading characteristics on the dynamic rupture process, *Eos Trans. AGU, Fall Meet. Suppl.*, **89**, no. 53, Abstract S51D-1798.
- Dalguer, L., H. Miyake, S. Day, and K. Irikura (2008). Surface rupturing and buried dynamic-rupture models calibrated with statistical observations of past earthquakes, *Bull. Seismol. Soc. Am.* **98**, no. 3, 1147–1161.
- Day, S., and C. Bradley (2001). Memory-efficient simulation of anelastic wave propagation, *Bull. Seismol. Soc. Am.* **91**, no. 3, 520–531.
- Day, S., and G. Ely (2002). Effect of a shallow weak zone on fault rupture: numerical simulation of scale-model experiments, *Bull. Seismol. Soc. Am.* **92**, no. 8, 3022–3041.
- Field, E. H. (1996). Spectral amplification in a sediment-filled valley exhibiting clear basin-edge-induced waves, *Bull. Seismol. Soc. Am.* **86**, 991–1005.
- Frankel, A., D. Carver, E. Cranswick, T. Bice, R. Sell, and S. Hanson (2001). Observations of basin ground motion from a dense seismic array in San Jose, California, *Bull. Seismol. Soc. Am.* **91**, 1–12.

- Fukuyama, E., T. Mikumo, and K. Olsen (2003). Estimation of the critical slip-weakening distance: Theoretical background, *Bull. Seismol. Soc. Am.* **93**, no. 4, 1835–1840.
- Guatteri, M., P. Mai, G. Beroza, and J. Boatwright (2003). Strong ground-motion prediction from stochastic-dynamic source models, *Bull. Seismol. Soc. Am.* **93**, no. 1, 301–313.
- Hallier, S., E. Chaljub, M. Bouchon, and H. Sekiguchi (2008). Revisiting the basin-edge effect at Kobe during the 1995 Hyogo-Ken Nanbu earthquake, *Pure Appl. Geophys.* **165**, 1751–1760.
- Hill, J., H. Benz, M. Murphy, and G. Schuster (1990). Propagation and resonance of *SH* waves in the Salt Lake Valley, Utah, *Bull. Seismol. Soc. Am.* **80**, no. 1, 23–42.
- Hunter, J. D. (2007). Matplotlib: A 2D graphics environment, *Comput. Sci. Eng.* **9**, 90–95.
- Kaneko, Y., N. Lapusta, and J. Ampuero (2008). Spectral element modeling of spontaneous earthquake rupture on rate and state faults: Effect of velocity-strengthening friction at shallow depths, *J. Geophys. Res.* **113**, B09317, doi: [10.1029/2007JB005553](https://doi.org/10.1029/2007JB005553).
- Kawase, H. (1996). The cause of the damage belt in Kobe: “The basin-edge effect, “Constructive interference of the direct *S*-wave with the basin-induced diffracted/rayleigh waves, *Seismol. Res. Lett.* **67**, no. 5, 25–34.
- Machette, M., S. Personius, A. Nelson, D. Schwartz, and W. Lund (1991). The Wasatch fault zone, Utah—Segmentation and history of Holocene earthquakes, *J. Struct. Geol.* **13**, no. 2, 137–149.
- Madariaga, R., K. Olsen, and R. Archuleta (1998). Modeling dynamic rupture in a 3D earthquake fault model, *Bull. Seismol. Soc. Am.* **88**, no. 5, 1182–1197.
- Magistrale, H., and S. Day (1999). 3D simulations of multi-segment thrust fault rupture, *Geophys. Res. Lett.* **26**, no. 14, 2093–2096.
- Magistrale, H., S. Day, R. Clayton, and R. Graves (2000). The SCEC southern California reference three-dimensional seismic velocity model version 2, *Bull. Seismol. Soc. Am.* **90**, no. 6B, S65–S76.
- Magistrale, H., K. Olsen, and J. Pechmann (2008). Construction and verification of a Wasatch Front community velocity model: Collaborative research with San Diego State University and the University of Utah, *U.S. Geol. Surv. Final Tech. Rept. Submitted to NEHRP*, 14 pp.
- Magistrale, H., J. Pechmann, and K. Olsen (2009). The Wasatch Front, Utah, community seismic velocity model, *Seismol. Res. Lett.* **80**, 368.
- Mai, P. M., and G. C. Beroza (2002). A spatial random field model to characterize complexity in earthquake slip, *J. Geophys. Res. (Solid Earth)* **107**, 2308–2328, doi: [10.1029/2001JB000588](https://doi.org/10.1029/2001JB000588).
- Mai, P., P. Spudich, and J. Boatwright (2005). Hypocenter locations in finite-source rupture models, *Bull. Seismol. Soc. Am.* **95**, no. 3, 965.
- McCalpin, J., and C. Nelson (2000). Long recurrence records from the Wasatch fault zone, *U.S. Geol. Surv. Final Tech. Rept.*, National Earthquake Hazards Reduction Program, Contract number 99HQGR0058.
- McCalpin, J., and S. Nishenko (1996). Holocene paleoseismicity, temporal clustering, and probabilities of future large ($M > 7$) earthquakes on the Wasatch fault zone, Utah, *J. Geophys. Res.* **101**, 6233–6253.
- McDonald, G., and F. Ashland (2008). *Earthquake Site Conditions in the Wasatch Front Urban Corridor*, Utah, Special Study 125 (Utah Geol. Surv.), Utah Geological Survey, Salt Lake City, 125 pp.
- Murphy, M., H. Benz, J. Hill, and G. Schuster (1988). Prediction of seismic amplification due to resonance of *P-SV* and *SH* waves in Salt Lake Valley, Utah, *Seismol. Res. Lett.* **59**, 10–11.
- O’Connell, D. R. H., S. Ma, and R. J. Archuleta (2007). Influence of dip and velocity heterogeneity on reverse- and normal-faulting rupture dynamics and near-fault ground motions, *Bull. Seismol. Soc. Am.* **97**, no. 6, 1970–1989.
- Olsen, K. B. (1994). Simulation of three-dimensional wave propagation in the Salt Lake basin, *Ph.D. Thesis*, University of Utah, Salt Lake City, Utah.
- Olsen, K., and R. Archuleta (1996). Three-dimensional simulation of earthquakes on the Los Angeles fault system, *Bull. Seismol. Soc. Am.* **86**, no. 3, 575–596.
- Olsen, K., and G. Schuster (1994). Three-dimensional modeling of the site amplification in East Great Salt Lake basin, *U.S. Geol. Surv. Tech. Rept. 1434-93-g-2345*, 102 pp.
- Olsen, K. B., and G. Schuster (1995). Causes of low-frequency ground motion amplification in the Salt Lake basin: The case of the vertically incident *P* wave, *Geophys. J. Int.* **122**, no. 3, 1045–1061.
- Olsen, K., J. C. Pechmann, and G. T. Schuster (1995). Simulation of 3D elastic wave propagation in the Salt Lake Basin, *Bull. Seismol. Soc. Am.* **85**, no. 6, 1688–1710.
- Olsen, K., J. Pechmann, and G. Schuster (1996). An analysis of simulated and observed blast records in the Salt Lake basin, *Bull. Seismol. Soc. Am.* **86**, 1061–1076.
- Olsen, K. B., S. M. Day, L. A. Dalgner, J. Mayhew, Y. Cui, J. Zhu, V. Cruz-Atienza, D. Roten, P. Maechling, T. Jordan, D. Okaya, and A. Chourasia (2009). ShakeOut-D: Ground motion estimates using an ensemble of large earthquakes on the southern San Andreas Fault with spontaneous rupture propagation, *Geophys. Res. Lett.* **36**, L04303, doi: [10.1029/2008GL036832](https://doi.org/10.1029/2008GL036832).
- OpenSHA (2010). Open seismic hazard analysis computer platform, <http://www.opensha.org> (last accessed May 2011).
- Pitarka, A., K. Irikura, T. Iwata, and H. Sekiguchi (1998). Three-dimensional simulation of the near-fault ground motion for the 1995 Hyogo-Ken Nanbu (Kobe), Japan, earthquake, *Bull. Seismol. Soc. Am.* **88**, no. 2, 428–440.
- Press, W., S. Teukolsky, W. Vetterling, and B. Flannery (2007). *Numerical Recipes: The Art of Scientific Computing*, Third Edition, Cambridge University Press, Cambridge, 1256 pp.
- Ripperger, J., J. Ampuero, P. M. Mai, and D. Giardini (2007). Earthquake source characteristics from dynamic rupture with constrained stochastic fault stress, *J. Geophys. Res. (Solid Earth)* **112**, B04311, doi: [10.1029/2006JB004515](https://doi.org/10.1029/2006JB004515).
- Ripperger, J., P. Mai, and J. Ampuero (2008). Variability of near-field ground motion from dynamic earthquake rupture simulations, *Bull. Seismol. Soc. Am.* **98**, no. 3, 1207–1228.
- Roten, D., D. Fäh, K. Olsen, and D. Giardini (2008). A comparison of observed and simulated site response in the Rhône valley, *Geophys. J. Int.* **173**, 958–978.
- Schmedes, J., R. Archuleta, and D. Lavallée (2010). Correlation of earthquake source parameters inferred from dynamic rupture simulations, *J. Geophys. Res.* **115**.
- Scholz, C. (1998). Earthquakes and friction laws, *Nature* **391**, no. 6662, 37–42.
- Schroeder, W., K. Martin, and B. Lørsensen (2006). *The Visualization Toolkit: An Object-Oriented Approach to 3D Graphics*, Fourth Edition, Kitware, Clifton Park, New York, 512 pp.
- Sibson, R. (1991). Loading faults to failure, *Bull. Seismol. Soc. Am.* **81**, no. 6, 2493–2497.
- Smith, R., and W. Arabasz (1991). Seismicity of the Intermountain seismic belt, in *Neotectonics of North America*, D. Slemmons, E. Engdahl, M. Zoback, and D. Blackwell (Editors), Geological Society of America, Boulder, Colorado, pp. 185–228.
- Solomon, B., N. Storey, I. Wong, N. Gregor, D. Wright, and G. McDonald (2004). Earthquake-hazards scenario for a $M 7$ earthquake on the Salt Lake City segment of the Wasatch fault zone, Utah, *Utah Geol. Surv. Special Study 111DM*, CD-ROM, 59 pp., 6 Plates.
- Somerville, P., and A. Pitarka (2006). Differences in earthquake source and ground motion characteristics between surface and buried earthquakes, in *Proc. of the Eighth National Conf. Earthq. Eng.*, San Francisco, 18–22 April.
- Wells, D., and K. Coppersmith (1994). New empirical relationships among magnitude, rupture length, rupture width, rupture area, and surface displacement, *Bull. Seismol. Soc. Am.* **84**, no. 4, 974–1002.
- Wessel, P., and W. Smith (1998). New, improved version of Generic Mapping Tools released, *Eos Trans. AGU* **79**, no. 47, 579.
- Wong, I., and W. Silva (1993). Site-specific strong ground motion estimates for the Salt Lake Valley, Utah, *Misc. Pub. 93-9, Utah Geol. Surv.*, 34 pp.

Wong, I., W. Silva, N. Gregor, D. Wright, F. Ashland, G. McDonald, S. Olig, G. Christenson, and B. Solomon (2002). Earthquake scenario ground shaking maps for the central Wasatch Front, Utah, in *Proc. Seventh U.S. Nat. Conf. Earthq. Eng.*, Boston, Massachusetts, 21–25 July.

Wong, I., W. Silva, S. Olig, P. Thomas, D. Wright, N. Ashland, N. Gregor, M. Pechmann, M. Dober, G. Christenson, and R. Gerth (2002). Earthquake scenario and probabilistic ground shaking maps for the Salt Lake City, Utah, metropolitan area, *Utah Geol. Surv. Misc. Pub. MP-02-5*, 50 pp.

Department of Geological Sciences
San Diego State University
5500 Campanile Dr.
San Diego, California 92182-1020
droten@sciences.sdsu.edu
(D.R., K.B.O., H.M.)

Department of Geology and Geophysics
University of Utah
115 South 1460 East, Room 383 FASB
Salt Lake City, Utah 84112-0102
(J.C.P.)

Universidad Nacional Autónoma de México
Instituto de Geofísica
Departamento de Sismología
Circuito de la Investigación Científica s/n
Ciudad Universitaria, 04510
México D.F. Mexico
(V.M.C.)

Manuscript received 26 January 2011